Data report: joint analysis of acoustic and magnetic susceptibility anisotropies in the Nankai accretionary prism[1]

Laurent Louis,[2,3] Fabien Humbert,[2] Philippe Robion,[2] Pierre Henry,[4] Matthew Knuth,[5] and William Likos[6]

Chapter contents

[1] Louis, L., Humbert, F., Robion, P., Henry, P., Knuth, M., and Likos, W., 2012. Data report: joint analysis of acoustic and magnetic susceptibility anisotropies in the Nankai accretionary prism. *In* Kinoshita, M., Tobin, H., Ashi, J., Kimura, G., Lallemant, S., Screaton, E.J., Curewitz, D., Masago, H., Moe, K.T., and the Expedition 314/315/316 Scientists, *Proc. IODP,* 314/315/316: Washington, DC (Integrated Ocean Drilling Program Management International, Inc.). doi:10.2204/iodp.proc.314315316.216.2012
[2] Département des Sciences de la Terre et l'Environnement, Université de Cergy-Pontoise, 95031 Cergy-Pontoise, France. Correspondence author: laurent.louis@bp.com
[3] BP America, Houston TX 77079, USA.
[4] CEREGE, Collège de France, 13545 Aix-en-Provence Cedex 04, France.
[5] Department of Geosciences, University of Wisconsin-Madison, Madison WI 53706, USA.
[6] Department of Civil and Environmental Engineering, University of Missouri, Columbia MO 65211, USA.

Abstract

This report presents the results of laboratory measurements on discrete samples from Integrated Ocean Drilling Program Expeditions 315 and 316 of the complex drilling project Nankai Trough Seismogenic Zone Experiment. Anisotropies of *P*-wave velocity and magnetic susceptibility were measured on a common suite of samples to evaluate the potential of acoustic anisotropy as a tool for deformation studies. Whereas in-plane *P*-wave velocity directions provide ambiguous results, the associated anisotropy parameter appears exempt from lithologic artifacts, in contrast to anisotropy of magnetic susceptibility, and overall agreement between the fabric shape parameter values suggests further exploratory work.

Introduction

Integrated Ocean Drilling Program (IODP) Expeditions 315 and 316 of the Nankai Trough Seismogenic Zone Experiment (NanTroSEIZE) complex drilling project were primarily dedicated to core sampling at multiple sites across the Kumano Basin region, offshore Kii Peninsula, Japan. Six relatively shallow sites (<1000 meters below seafloor [mbsf]) were successfully cored and sampled along a transect from the Kumano forearc basin (Site C0002) to the frontal thrust of the Nankai accretionary prism (Sites C0006 and C0007), including cores taken from the shallow portion of a major out-of-sequence thrust fault (megasplay) (Sites C0001, C0004, and C0008) (Fig. F1).

This report presents the results of a pilot study intended to evaluate the potential of using anisotropy of *P*-wave velocity (APV) as a complementary tool for deformation studies. This evaluation was performed through a sample-to-sample comparison between APV and the commonly used anisotropy of magnetic susceptibility (AMS) parameter.

Whereas AMS is sensitive to magnetic mineral fabric, *P*-wave velocity may illuminate the mechanical history of sedimentary rock by its sensitivity to pore space, grain alignment, the nature of intergranular contacts, and damage features such as microcracks. In particular, changes in clay platelet alignment and pore space anisotropy in response to tectonic stress, which have been shown to significantly influence electrical conductivity (Henry et al., 2003), are also likely to have an effect on *P*-wave velocity. Many studies have focused on microstructural control of APV (e.g., Lo et

doi:10.2204/iodp.proc.314315316.216.2012

al., 1986; Kern, 1993; Johnston and Christensen, 1995; Hornby, 1998; Louis et al., 2003, 2004, 2005), including work related to IODP expeditions (Brückmann et al., 1993, 1997). However, its potential use as a structural tool has received limited attention (Hrouda et al., 1993; Siegesmund et al., 1993; Louis et al., 2006, 2008; Amrouch et al., 2010). The data presented here supplement the shipboard physical property measurements performed during Expeditions 315 and 316 (see site chapters in this volume).

Sampling and preparation

Before being sent to the onshore laboratory for further investigations, samples were shaped onboard the D/V *Chikyu* into ~20 mm thick cubes with a parallel diamond blade saw and measured for electrical conductivity and APV. In most cases, the orientation convention used for paleomagnetism was followed: $+z$ points downcore along the core axis, $+x$ points into the working half, and $+y$ is perpendicular to the z-axis within the core face. Once received, samples were measured for magnetic remanence in order to allow azimuthal reorientation, were left at room temperature for several days, and then were shaped into polyhedrons before being measured for AMS and APV. Polyhedrons with 14 facets were prepared to allow *P*-wave velocity measurement in seven independent directions, as opposed to three directions in the original cubes. The seven directions measured consist of the three reference directions plus four diagonals (Fig. **F2**). For numerous reasons from recovery issues to orientation, drying, and preparation of the facets, a significant number of samples had to be discarded, and not all units cored are represented in this study. Our data set comprises 262 samples for AMS and 185 samples for APV. Individual counts per site for both measurements are given in Figure **F1.**

Methods

Sample reorientation

Samples were azimuthally reoriented through stepwise demagnetization of the viscous remanent magnetization (VRM) acquired in an ambient magnetic field. Demagnetization was conducted at the École Normale Supérieure de Paris (France) for samples from Sites C0001, C0002, C0007, and C0008 and at CEREGE in Aix-en-Provence (France) for samples from Sites C0004 and C0006. Both facilities use a superconducting quantum interference device (SQUID) magnetometer with horizontal sensors, and the measurement protocol consists of demagnetization increments of 2–10 mT, up to 60 mT. The resulting data were processed using Zijderveld diagrams (Zijderveld, 1967). In most cases, samples exhibit low-coercivity magnetization between 0 and 10 mT with a subvertical slope, attributed to the rotary motion of the coring device, and medium-coercivity magnetization between 10 (or 20) and 40 mT with a mean inclination near 33°, which was used for reorientation.

Anisotropy of magnetic susceptibility

The AMS was measured with a susceptibility bridge AGICO KLY3S, which has a sensitivity of 3×10^{-8} SI. The system measures the induced magnetization (M) of a specimen inside a coil that generates a low alternating field (H). If the magnitude of the magnetization field is on the same order as that of the Earth's magnetic field, then M and H are approximately linearly related according to $M_i = K_{ij} \times H_j$, where K_{ij} is a second-rank symmetric tensor representing the magnetic susceptibility (Nye, 1957; Daly, 1970). The eigenvalues of the magnetic susceptibility tensor (K_{ij}) are denoted by K_1, K_2, and K_3, with $K_1 > K_2 > K_3$. The anisotropy and shape of the susceptibility ellipsoid are quantified using the parameters P_j and T_j (Jelinek, 1981). Their mathematical expressions are as follows:

$$P_j = \exp\sqrt{2\left[\left(\ln\frac{K_1}{K_m}\right)^2 + \left(\ln\frac{K_2}{K_m}\right)^2 + \left(\ln\frac{K_3}{K_m}\right)^2\right]}$$

and

$$T_j = \frac{\ln(K_2/K_3) - \ln(K_1/K_2)}{\ln(K_2/K_3) + \ln(K_1/K_2)},$$

where K_m is the mean magnetic susceptibility. The anisotropy parameter (P_j) is typically a measure of the eccentricity of the AMS ellipsoid, and the shape parameter (T_j) is negative ($-1 < T_j < 0$) when the fabric is linear (or prolate) and positive ($0 < T_j < 1$) when the fabric is planar (or oblate) (Jelinek, 1981; Borradaile and Henry, 1997).

Anisotropy of *P*-wave velocity

Ultrasonic *P*-wave velocities were measured with a pulse generator Panametrics 5058 PR with up to 900 V output voltage, two *P*-wave transducers with a resonance frequency of 0.5 MHz, and a digital oscilloscope HP54603B connected to a PC for data collection. For every sample, the thickness across each of the seven sets of parallel facets was measured, and then the *P*-wave time-of-flight across each length was determined by picking the first arrival on the oscilloscope. Once the *P*-wave velocities were calculated, a best fitting second-order symmetric tensor was retrieved in the same fashion as for magnetic susceptibility, following the method proposed by Louis et al. (2004) and based on the assumption of elliptical anisotropy (Thomsen, 1986; Tsvankin,

1997). Because the inversion yields three principal directions and values, the same anisotropy and shape parameters as those used for the AMS data (i.e., P_j and T_j) were calculated, providing a direct and simple way of comparing both data sets. The eigenvalues of the *P*-wave velocity pseudotensor are denoted by V_1, V_2, and V_3, with $V_1 > V_2 > V_3$.

The results of the magnetic susceptibility and *P*-wave velocity measurements are reported in Table T1 as the mean, anisotropy parameter P_j, and shape parameter T_j for each property.

Results

Bulk analysis

Although variations in the anisotropy of a physical property may often, at least qualitatively, be attributed to strain, subtle lithologic changes may greatly affect observed anisotropies through contrasting contributions from individual components. Upon changes in their relative amounts, a binary mixture of two components with contrasting intrinsic properties and anisotropies may cause fluctuations of the total effective anisotropy without this anisotropy being at all related to strain. In the case of magnetic susceptibility, because K_m is usually considered a proxy for rock composition, comparison between K_m and P_j can serve as a test of the mineralogical control over magnetic anisotropy (Borradaile and Henry, 1997). Figure F3A is a semilog plot of P_j vs. K_m for all of our samples. Overall, the values for K_m vary considerably from ~80 × 10^{-6} to ~5000 × 10^{-6}, and an apparent positive correlation was observed past a transition range between 200 × 10^{-6} and 300 × 10^{-6}, below which no systematic effect of K_m over P_j is apparent. The high susceptibility values observed in some units at Sites C0006, C0007, C0008, and to a lesser extent at Site C0004, were attributed to the presence of numerous volcanic ash and sand layers (see the "Site C0004," "Site C0006," "Site C0007," and "Site C0008" chapters [Expedition 316 Scientists, 2009a, 2009b, 2009c, 2009d]). These variations in magnetic susceptibility, which were found to closely parallel natural magnetic remanence, are more specifically caused by variable contents of magnetite (Kitamura et al., 2010). The P_j vs. K_m semilog plot suggests a value of ~250 × 10^{-6} for the divide between paramagnetic-dominated and ferromagnetic-influenced signals, which is consistent with reference data obtained for paramagnetic rocks and minerals (Rochette et al., 1992; Borradaile and Henry, 1997; Martín-Hernández and Hirt, 2003).

The same plot as that drawn for magnetic susceptibility is shown in Figure F3B for *P*-wave velocity data. In this case, one could expect *P*-wave velocity anisotropy to show contrasting sensitivity to various components, a good example of which would be the presence of a network of microcracks. For our samples, however, no particular pattern is evident. Except for Site C0002, all data remain in the same anisotropy range regardless of the average *P*-wave velocity measured on the sample.

Physical property fabrics

A common approach to interpreting AMS ellipsoids in terms of strain consists of plotting Jelinek parameters P_j and T_j against one another (Tarling and Hrouda, 1993). Whereas the eccentricity value provided by P_j is an indication of the extent to which a given fabric is developed, the shape parameter T_j, which is basically the relative difference between the foliation parameter $F = K_2/K_3$ and the lineation parameter $L = K_1/K_2$, defines that fabric as either linear (prolate) or planar (oblate). For sedimentary rocks, and mud rocks in particular, progressive overprinting of a tectonic fabric on an initial sedimentary fabric is often qualitatively described by a path initiating at the top of the oblate field (T_j ~ 1), decreasing in both P_j and T_j to reflect the destruction of the initial sedimentary fabric by subhorizontal shortening and then, after reaching a minimum in P_j and T_j, increasing for both parameters with the formation of a new foliation oriented perpendicular to the initial one (Borradaile and Henry, 1997; Parés, 2004). Such a T_j vs. P_j plot is shown in Figure F4A for our AMS data. Overall, the two parameters seem to roughly correlate, although the artifact on P_j associated with variable content in magnetite considerably affects the plot and precludes comparison between drilled sites in term of strain intensity.

We show in Figure F4B a T_j vs. P_j plot for *P*-wave velocity data. As for AMS, most data are located in the oblate domain. Values from all sites seem, however, to participate in the same initial stage of the strain path defined earlier (joint decrease of the two parameters initiating from a highly oblate fabric). Three zones can be distinguished within this plot: (1) a domain that comprises mostly samples from Site C0002 with *P*-wave anisotropy > 1.2 and clearly oblate fabrics with $T_j > 0.4$, (2) a domain where most samples from other sites have anisotropy values of $P_j \leq 1.2$ and still oblate fabrics with $0 \leq T_j \leq 0.6$, and (3) a low-anisotropy and prolate fabric domain with $P_j \leq 1.2$ and $T_j < 0$. Following similar reasoning as for AMS, the first domain seems to correspond to samples that have been vertically compacted with low net disturbance by horizontal shortening. On the other end of the path, where the values of T_j become

negative, samples may be considered to be most affected by horizontal shortening. Although such representation and corresponding interpretation have, to our knowledge, never been applied to *P*-wave velocity data, one can expect from APV a response similar to AMS in poorly consolidated material with high porosity. In the samples studied here, two major sources of *P*-wave anisotropy should be taken into account: the degree of alignment of the constituting phyllosilicates (see Johnston and Christensen, 1995) and the preferential orientation of pore space (an example of such an effect can be found in Louis et al., 2003). Therefore, the conceptual mechanisms of rotation of platy particles under uniaxial stress essentially apply to both AMS and APV, with the difference that preferential orientation of the pore space may cause the *P*-wave velocity to exhibit higher anisotropies than AMS, as seems to occur in Figures F3 and F4. The fact that (1) both assumed sources of anisotropy for *P*-wave velocity are expected to evolve in conjunction upon vertical compaction or horizontal shortening and (2) from a poroelastic viewpoint the microstructure is devoid of features capable of overriding the background signal, as is the case for the magnetic mineralogy, suggests that the conceptual strain path may in fact be better fitted with APV data than with AMS data when considering the entire structure. In this framework, Figure F4B suggests gradual progression from globally compacted sediments (of which the sample batch at Site C0002 is a good example) to material increasingly affected by lateral shortening. Using the terminology of Borradaile and Henry (1997), samples from NanTroSEIZE Expeditions 315 and 316 exhibit sedimentary to transitional fabrics.

Tectonic implications

Figure F5 depicts equal-area lower hemisphere projections of the AMS and APV eigenvectors corresponding to the maximum (solid black squares) and minimum (solid red circles) values after paleomagnetic reorientation for all sites. Sample groups are generally defined according to the lithologic units, except for Sites C0004 and C0006, where subgroups were used. For every (sub)group, the depth interval covered by the samples is reported on the top left corner of the AMS plot. On each plot, the average value of T_j is also provided, together with the direction of maximum horizontal stress derived for the same intervals by Chang et al. (2010) using borehole breakouts, when available. Open symbols for eigenvectors correspond to samples with either very low anisotropy or evident misorientation for both AMS and APV. Some intervals such as the hanging wall of the splay fault at Site C0004 could not be included because samples were obtained from randomly oriented core fragments.

Using AMS plots as a reference, three types of fabrics can be observed: sedimentary, transitional with sedimentary relicts (K_1 oriented parallel to the structural axis and K_3 oriented perpendicular to the bedding), and transitional with K_3 axis rotating toward the shortening direction. Not all projections exhibit straightforward patterns. However, some general observations can be made concerning their apparent relationship to deformation. At Sites C0002 and C0008, slope sediments display essentially sedimentary fabrics with subvertical K_3 directions and no clear grouping of K_1 directions. On the opposite end of the spectrum, most evolved fabrics are found at Site C0001 in the hanging wall of the megasplay fault and within the Shikoku Basin facies sediments at Sites C0006 and C0007 (Unit III). This last observation is consistent with the findings of Kitamura et al. (2010). Finally, intermediate fabrics with K_1 grouping approximately parallel to the structures and subvertical K_3 directions are observed in the underthrust sediments at Site C0004 and in Unit II of Sites C0006 and C0007. These fabrics are virtually identical to the ones observed by Owens (1993) at Ocean Drilling Program (ODP) Site 808. In all cases where clustering of K_1 is observed, there is a good geometric agreement with the maximum horizontal stress direction of Chang et al. (2010).

The one-to-one comparison between AMS and APV plots is inconclusive at this stage. Generally, minimum *P*-wave velocities are found along the vertical direction, and in some cases, clustering of the maximum velocity (V_1) directions is observed (Site C0004 and mid-interval at Site C0006), albeit with certain angular offsets with respect to AMS, that could be related to the presence of some localized deformation feature. Although this result suggests that APV may not be a strong directional marker, the T_j values obtained from APV and AMS for the intervals shown in Figure F5 are in good agreement, as shown in Figure F6. Here, T_j values are averaged per interval with standard deviation for the error bar. The values for P_j were not used because of their observed sensitivity to the magnetic mineralogy (Fig. F4A). In Figure F6, T_j values for APV and AMS data are located close to the 1:1 correlation line. The zones most likely affected by lateral compaction at Site C0001 (megasplay hanging wall) and in the Shikoku Basin facies sediments of Sites C0006 and C0007 (frontal thrust), are confirmed by low average T_j values for both AMS and APV. In contrast, the two Site C0002 units (solid red circles) on top of the plotted data are apparently the ones with the most preserved sedimentary fabrics.

Comparison of values for Site C0004 underthrust sediments with Site C0008 slope sediments suggests that splay fault activity did not result in further vertical compaction. On the contrary, the shallower of the two Site C0004 subunits exhibits a relatively low T_j value suggestive of horizontal shortening, which might be due to presently acting horizontal stress underneath the megasplay.

Acknowledgments

This study used samples provided by the Integrated Ocean Drilling Program (IODP). Funding for this research came in part from the French INSU–CNRS 3F (Failles, Fluides, Flux) program. We thank Julie Carlut at École Normale Supérieure (Paris, France) and Jerome Gattacceca and Pierre Rochette at CEREGE (Aix-en-Provence, France) for making their facilities available and for helping with magnetic remanence measurements. We also thank Alexandra Renard at the Université de Cergy-Pontoise for participating in the physical property measurements. This manuscript was improved thanks to the careful review of Xixi Zhao and suggestions by Daniel Curewitz.

References

Amrouch, K., Robion, P., Callot, J.-P., Lacombe, O., Daniel, J.-M., Bellahsen, N., and Faure, J.-L., 2010. Constraints on deformation mechanisms during folding provided by rock physical properties: a case study at Sheep Mountain anticline (Wyoming, USA). *Geophys. J. Int.,* 182(3):1105–1123. **doi:10.1111/j.1365-246X.2010.04673.x**

Borradaile, G.J., and Henry, B., 1997. Tectonic applications of magnetic susceptibility and its anisotropy. *Earth-Sci. Rev.,* 42(1–2):49–93. **doi:10.1016/S0012-8252(96)00044-X**

Brückmann, W., Moran, K., and Housen, B.A., 1997. Directional properties of *P*-wave velocities and acoustic anisotropy in different structural domains of the northern Barbados Ridge accretionary complex. *In* Shipley, T.H., Ogawa, Y., Blum, P., and Bahr, J.M. (Eds.), *Proc. ODP, Sci. Results,* 156: College Station, TX (Ocean Drilling Program), 115–124. **doi:10.2973/odp.proc.sr.156.017.1997**

Brückmann, W., Moran, K., and Taylor, E., 1993. Acoustic anisotropy and microfabric development in accreted sediment from the Nankai Trough. *In* Hill, I.A., Taira, A., Firth, J.V., et al., *Proc. ODP, Sci. Results,* 131: College Station, TX (Ocean Drilling Program), 221–233. **doi:10.2973/odp.proc.sr.131.121.1993**

Chang, C., McNeill, L.C., Moore, J.C., Lin, W., Conin, M., and Yamada, Y., 2010. In situ stress state in the Nankai accretionary wedge estimated from borehole wall failures. *Geochem., Geophys., Geosyst.,* 11:Q0AD04–Q0AD20. **doi:10.1029/2010GC003261**

Daly, L., 1970. Étude des propriétés magnétiques des roches métamorphiques ou simplement tectonisées. Nature de leur aimantation naturelle. Détermination de leur anisotropie magnétique et application à l'analyse [Thèse Doctorat d'État]. Univ. Paris.

Expedition 316 Scientists, 2009a. Expedition 316 Site C0004. *In* Kinoshita, M., Tobin, H., Ashi, J., Kimura, G., Lallemant, S., Screaton, E.J., Curewitz, D., Masago, H., Moe, K.T., and the Expedition 314/315/316 Scientists, *Proc. IODP,* 314/315/316: Washington, DC (Integrated Ocean Drilling Program Management International, Inc.). **doi:10.2204/iodp.proc.314315316.133.2009**

Expedition 316 Scientists, 2009b. Expedition 316 Site C0006. *In* Kinoshita, M., Tobin, H., Ashi, J., Kimura, G., Lallemant, S., Screaton, E.J., Curewitz, D., Masago, H., Moe, K.T., and the Expedition 314/315/316 Scientists, *Proc. IODP,* 314/315/316: Washington, DC (Integrated Ocean Drilling Program Management International, Inc.). **doi:10.2204/iodp.proc.314315316.134.2009**

Expedition 316 Scientists, 2009c. Expedition 316 Site C0007. *In* Kinoshita, M., Tobin, H., Ashi, J., Kimura, G., Lallemant, S., Screaton, E.J., Curewitz, D., Masago, H., Moe, K.T., and the Expedition 314/315/316 Scientists, *Proc. IODP,* 314/315/316: Washington, DC (Integrated Ocean Drilling Program Management International, Inc.). **doi:10.2204/iodp.proc.314315316.135.2009**

Expedition 316 Scientists, 2009d. Expedition 316 Site C0008. *In* Kinoshita, M., Tobin, H., Ashi, J., Kimura, G., Lallemant, S., Screaton, E.J., Curewitz, D., Masago, H., Moe, K.T., and the Expedition 314/315/316 Scientists, *Proc. IODP,* 314/315/316: Washington, DC (Integrated Ocean Drilling Program Management International, Inc.). **doi:10.2204/iodp.proc.314315316.136.2009**

Henry, P., Jouniaux, L., Screaton, E.J., Hunze, S., and Saffer, D.M., 2003. Anisotropy of electrical conductivity record of initial strain at the toe of the Nankai accretionary wedge. *J. Geophys. Res., [Solid Earth],* 108(B9):2407–2418. **doi:10.1029/2002JB002287**

Hornby, B.E., 1998. Experimental laboratory determination of the dynamic elastic properties of wet, drained shales. *J. Geophys. Res., [Solid Earth],* 103(B12):29945–29964. **doi:10.1029/97JB02380**

Hrouda, F., Pros, Z., and Wohlgemuth, J., 1993. Development of magnetic and elastic anisotropies in slates during progressive deformation. *Phys. Earth Planet. Inter.,* 77(3–4)251–265. **doi:10.1016/0031-9201(93)90102-F**

Jelinek, V., 1981. Characterization of the magnetic fabric of rocks. *Tectonophysics,* 79(3–4):T63–T67. **doi:10.1016/0040-1951(81)90110-4**

Johnston, J.E., and Christensen, N.I., 1995. Seismic anisotropy of shales. *J. Geophys. Res., [Solid Earth],* 100(B4):5991–6003. **doi:10.1029/95JB00031**

Kern, H., 1993. *P*- and S-wave anisotropy and shear-wave splitting at pressure and temperature in possible mantle rocks and their relation to the rock fabric. *Phys. Earth Planet. Inter.,* 78(3–4):245–256. **doi:10.1016/0031-9201(93)90159-7**

Kitamura, Y., Kanamatsu, T., and Zhao, X., 2010. Structural evolution in accretionary prism toe revealed by magnetic fabric analysis from IODP NanTroSEIZE Expedi-

tion 316. *Earth Planet. Sci. Lett.,* 292(1–2):221–230. **doi:10.1016/j.epsl.2010.01.040**

Lo, T., Coyner, K.B., and Toksöz, M.N., 1986. Experimental determination of elastic anisotropy of Berea sandstone, Chicopee shale, and Chelmsford granite. *Geophysics,* 51(1):164–171. **doi:10.1190/1.1442029**

Louis, L., Chen, T.-M.N., David, C., Robion, P., Wong, T., and Song, S., 2008. Anisotropy of magnetic susceptibility and *P*-wave velocity in core samples from the Taiwan Chelungpu-Fault Drilling Project (TCDP). *J. Struct. Geol.,* 30(8):948–962. **doi:10.1016/j.jsg.2008.03.006**

Louis, L., David, C., Metz, V., Robion, P., Menéndez, B., and Kissel, C., 2005. Microstructural control on the anisotropy of elastic and transport properties in undeformed sandstones. *Int. J. Rock Mech. Min. Sci.,* 42(7–8):911–923. **doi:10.1016/j.ijrmms.2005.05.004**

Louis, L., David, C., and Robion, P., 2003. Comparison of the anisotropic behaviour of undeformed sandstones under dry and saturated conditions. *Tectonophysics,* 370(1–4):193–212. **doi:10.1016/S0040-1951(03)00186-0**

Louis, L., Robion, P., and David, C., 2004. A single method for the inversion of anisotropic data sets with application to structural studies. *J. Struct. Geol.,* 26(11):2065–2072. **doi:10.1016/j.jsg.2004.03.005**

Louis, L., Robion, P., David, C., and Frizon de Lamotte, D., 2006. Multiscale anisotropy controlled by folding: the example of the Chaudrons fold (Corbières, France). *J. Struct. Geol.,* 28(4):549–560. **doi:10.1016/j.jsg.2006.01.002**

Martín-Hernández, F., and Hirt, A.M., 2003. The anisotropy of magnetic susceptibility in biotite, muscovite and chlorite single crystals. *Tectonophysics,* 367(1–2):13–28. **doi:10.1016/S0040-1951(03)00127-6**

Moore, G.F., Park, J.-O., Bangs, N.L., Gulick, S.P., Tobin, H.J., Nakamura, Y., Sato, S., Tsuji, T., Yoro, T., Tanaka, H., Uraki, S., Kido, Y., Sanada, Y., Kuramoto, S., and Taira, A., 2009. Structural and seismic stratigraphic framework of the NanTroSEIZE Stage 1 transect. *In* Kinoshita, M., Tobin, H., Ashi, J., Kimura, G., Lallemant, S., Screaton, E.J., Curewitz, D., Masago, H., Moe, K.T., and the Expedition 314/315/316 Scientists, *Proc. IODP,* 314/315/316: Washington, DC (Integrated Ocean Drilling Program Management International, Inc.). **doi:10.2204/iodp.proc.314315316.102.2009**

Nye, J.F., 1957. *Physical Properties of Crystals: Their Representation by Tensors and Matrices:* New York (Oxford Univ. Press).

Owens, W.H., 1993. Magnetic fabric studies of samples from Hole 808C, Nankai Trough. *In* Hill, I.A., Taira, A., Firth, J.V., et al., *Proc. ODP, Sci. Results,* 131: College Station, TX (Ocean Drilling Program), 301–310. **doi:10.2973/odp.proc.sr.131.130.1993**

Parés, J.M., 2004. How deformed are weakly deformed mudrocks? Insights from magnetic anisotropy. *Geol. Soc. Spec. Publ.,* 238(1):191–203. **doi:10.1144/GSL.SP.2004.238.01.13**

Rochette, P., Jackson, M., and Aubourg, C., 1992. Rock magnetism and the interpretation of anisotropy of magnetic susceptibility. *Rev. Geophys.,* 30(3):209–226. **doi:10.1029/92RG00733**

Siegesmund, S., Vollbrecht, A., and Pros, Z., 1993. Fabric changes and their influence on *P*-wave velocity patterns—examples from a polyphase deformed orthogneiss. *Tectonophysics,* 225(4):477–492. **doi:10.1016/0040-1951(93)90311-7**

Tarling, D.H., and Hrouda, F., 1993. *The Magnetic Anisotropy of Rocks:* London (Chapman and Hall).

Thomsen, L., 1986. Weak elastic anisotropy. *Geophysics,* 51(10):1954–1966. **doi:10.1190/1.1442051**

Tsvankin, I., 1997. Anisotropic parameters and *P*-wave velocity for orthorhombic media. *Geophysics,* 62(4):1292–1309. **doi:10.1190/1.1444231**

Zijderveld, J.D.A., 1967. AC demagnetization of rocks: analysis of results. *In* Collinson, D.W., Creer, K.M., and Runcorn, S.K. (Eds.), *Methods in Palaeomagnetism:* Amsterdam (Elsevier), 254–286.

Initial receipt: 21 December 2010
Acceptance: 19 October 2011
Publication: 23 January 2012
MS 314315316-216

Figure F1. Interpreted cross section of the Kumano transect (after **Moore et al., 2009**) and projected location of drilled sites. AMS = anisotropy of magnetic susceptibility, APV = anisotropy of *P*-wave velocity. BSR = bottom-simulating reflector. PTZ = protothrust zone. VE = vertical exaggeration.

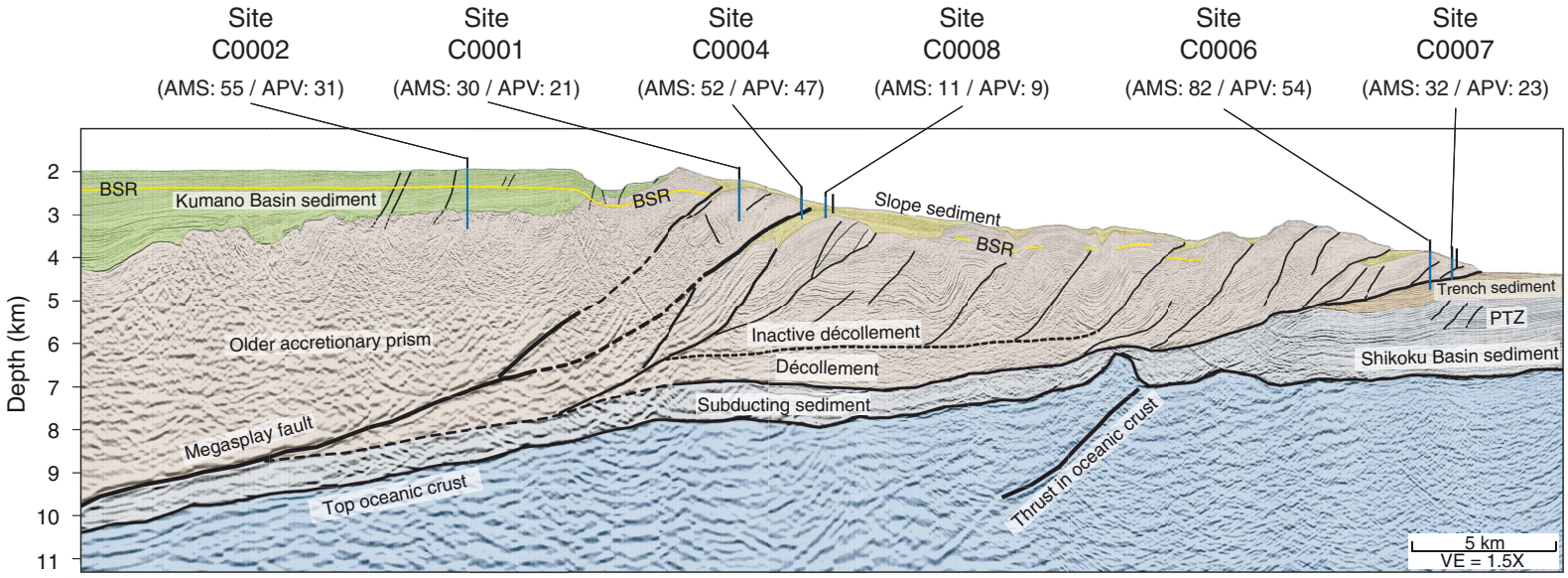

Figure F2. Photograph of discrete sample after preparation of 14 facets for *P*-wave velocity measurements.

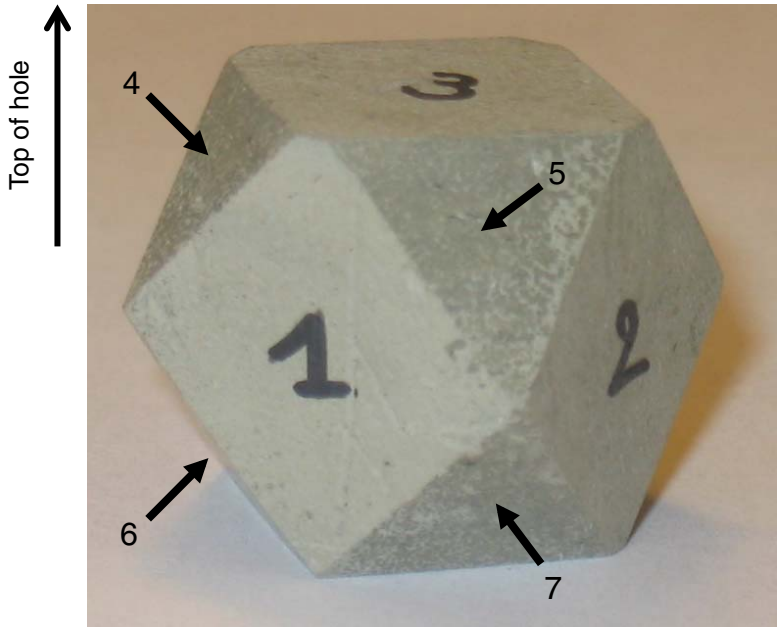

Figure F3. A. Jelinek anisotropy parameter (P_j) vs. mean magnetic susceptibility (K_m). **B.** Jelinek anisotropy parameter (P_j) vs. mean *P*-wave velocity (V_m). Data labels are ordered according to a northwest–southeast profile.

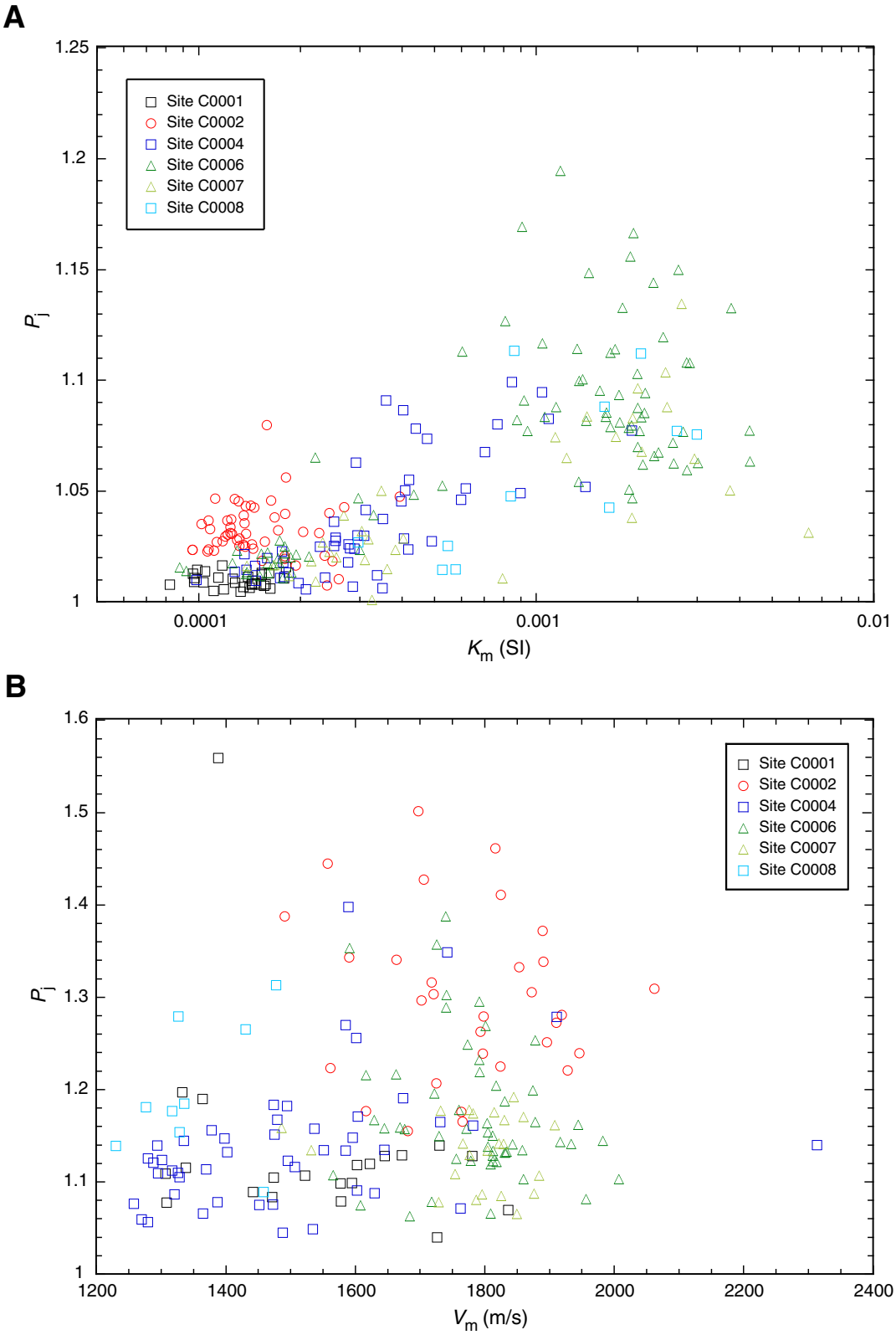

Figure F4. A. Jelinek shape parameter (T_j) vs. anisotropy parameter (P_j) for magnetic susceptibility. **B.** Jelinek shape parameter (T_j) vs. anisotropy parameter (P_j) for *P*-wave velocity. Data labels are ordered according to a northwest–southeast profile.

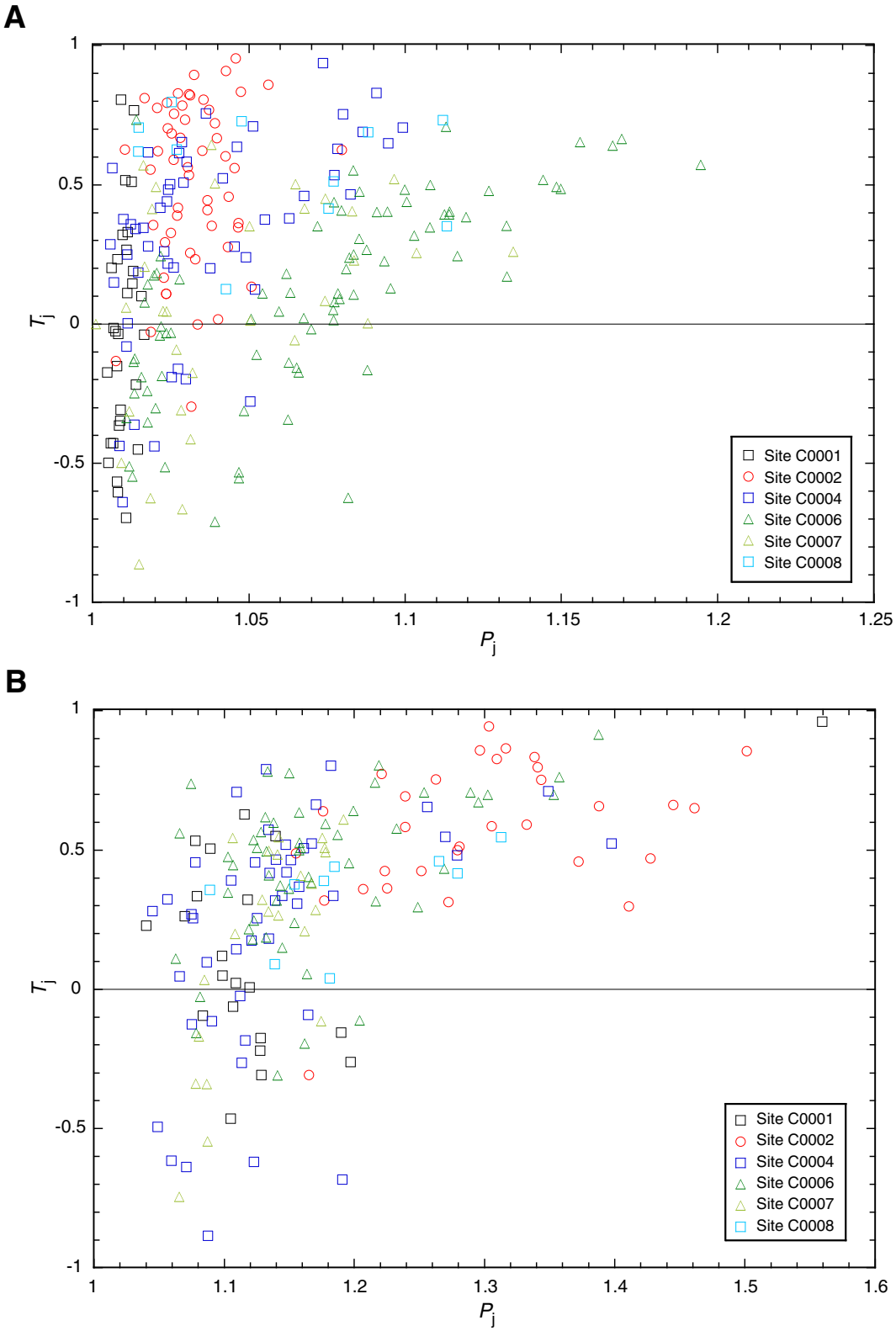

Figure F5. Lower hemisphere stereoplots for anisotropy of magnetic susceptibility (AMS) and anisotropy of *P*-wave velocity (APV) eigenvectors distributed by site and (sub)unit. The depth range in meters below seafloor (mbsf) for each pair of plots is provided at the top left corner of the AMS plots, and the average T_j value for each interval is provided at the top right corner of every plot. Arrows indicate maximum horizontal stress derived from borehole breakouts by Chang et al. (2010), when available. Solid black squares = direction of maximum value, solid red circles = direction of minimum value. Open symbols correspond to very low anisotropies or specimens with evident misorientations. BSR = bottom-simulating reflector. PTZ = protothrust zone. VE = vertical exaggeration.

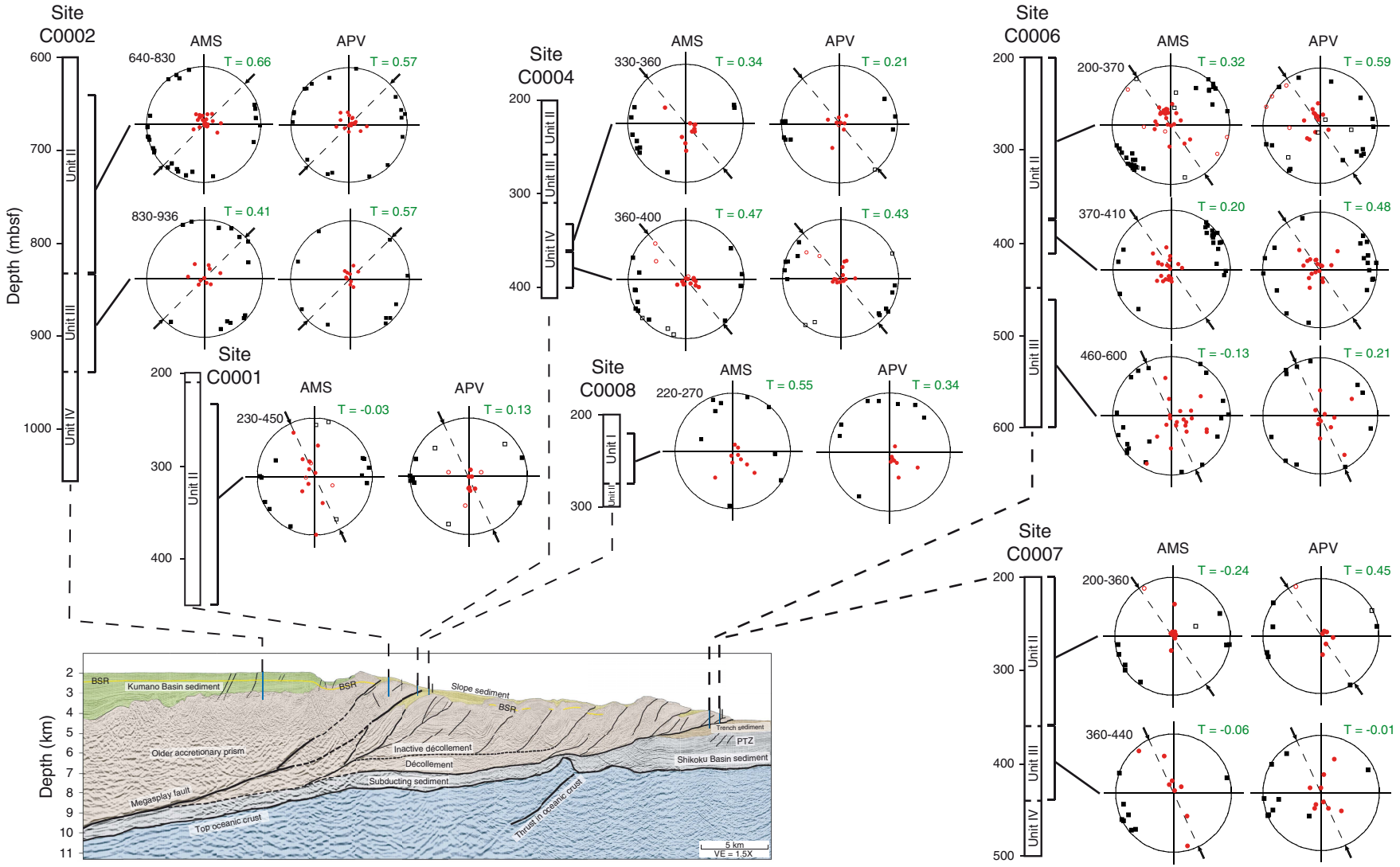

Figure F6. Interval-wise comparison between T_j values obtained from anisotropy of magnetic susceptibility (AMS; *x*-axis) and anisotropy of *P*-wave velocity (APV; *y*-axis), with error bars for standard deviations.

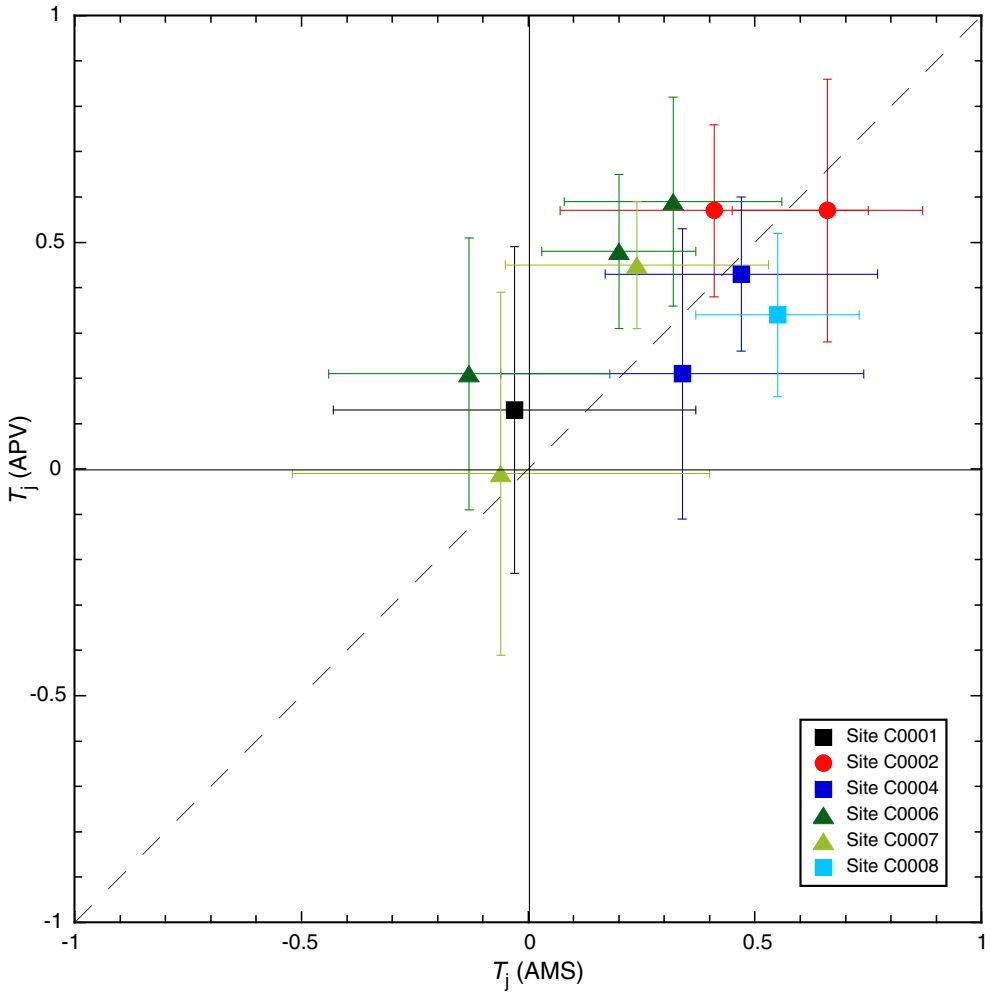

Table T1. Summary of physical properties measurements. (Continued on next four pages.)

Core, section, interval (cm)	Depth (mbsf)	AMS			APV		
		K_m (10^{-6} SI)	P_j	T_j	V_m (km/s)	P_j	T_j
315-C0001H-							
1R-2, 48–50	231.91	99	1.01	–0.45	—	—	—
2R-1, 26–28	239.76	110.9	1.01	–0.50	—	—	—
2R-3, 124–126	243.56	97.02	1.01	0.81	1.31	1.11	0.02
2R-4, 127–129	245.00	82.21	1.01	0.23	1.31	1.08	0.53
3R-1, 96–98	249.96	104.4	1.01	–0.22	1.34	1.12	0.63
3R-5, 24–26	253.47	97.26	1.01	0.27	1.36	1.19	–0.16
4R-1, 99–101	259.49	118.8	1.01	–0.43	1.44	1.09	0.50
4R-3, 61–63	261.93	126.1	1.01	0.52	1.39	1.56	0.96
5R-4, 49–51	271.34	133	1.00	–0.17	—	—	—
6R-1, 46–48	277.96	114.3	1.01	0.11	1.47	1.10	–0.47
6R-3, 42–44	279.34	96.1	1.01	0.15	—	—	—
7R-6, 15–17	292.84	144.3	1.01	0.32	—	—	—
7R-8, 44–46	295.95	128.1	1.01	–0.35	1.47	1.08	–0.09
8R-2, 79–81	298.70	135.6	1.01	–0.01	—	—	—
10R-3, 5–7	314.91	117.6	1.02	–0.04	—	—	—
11R-7, 20–22	328.89	—	—	—	1.33	1.20	–0.26
12R-2, 72–74	333.13	143.4	1.01	–0.57	1.52	1.11	–0.06
13R-7, 40–42	347.96	161.6	1.01	0.19	1.59	1.10	0.05
14R-3, 68–70	353.51	143.7	1.01	–0.04	1.62	1.12	0.01
15R-1, 52–54	360.02	140	1.01	0.33	1.60	1.12	0.32
16R-2, 65–67	371.07	178.7	1.01	–0.70	1.58	1.10	0.12
18R-4, 52–54	391.36	141.5	1.01	–0.43	1.58	1.08	0.33
19R-2, 6–8	398.98	157.8	1.01	–0.60	1.65	1.13	–0.18
21R-2, 9–11	414.00	146.4	1.01	–0.36	—	—	—
22R-1, 93–94	420.43	181.6	1.02	0.10	1.67	1.13	–0.31
23R-1, 66–68	429.66	153.8	1.01	0.77	1.73	1.14	0.55
23R-1, 66–68	429.66	153.9	1.01	0.51	—	—	—
24R-1, 117–119	438.67	103.4	1.01	–0.31	—	—	—
24R-3, 45–47	440.80	163.1	1.01	0.20	1.84	1.07	0.26
25R-1, 73–75	447.93	156	1.01	–0.03	1.73	1.04	0.23
25R-2, 17–19	447.93	152.9	1.01	–0.15	1.78	1.13	–0.22
315-C0002B-							
17R-4, 16–18	622.89	—	—	—	1.49	1.39	0.66
20R-1, 99–101	648.00	107.00	1.02	0.80	—	—	—
20R-3, 124–126	651.08	125.00	1.04	0.77	—	—	—
21R-2, 92–94	658.84	172.00	1.03	0.90	—	—	—
21R-4, 122–124	660.54	270.00	1.04	0.91	1.59	1.34	0.75
22R-1, 6–8	666.07	236.00	1.02	0.62	—	—	—
23R-2, 126–128	677.68	249.00	1.02	0.55	1.77	1.17	–0.31
23R-4, 60–62	678.85	394.00	1.05	0.83	1.71	1.43	0.47
24R-1, 87–89	685.38	136.00	1.04	0.72	1.66	1.34	0.80
24R-3, 68–70	687.02	130.00	1.03	0.67	—	—	—
25R-1, 126–128	695.27	145.00	1.02	0.70	—	—	—
26R-1, 122–124	704.73	144.00	1.03	0.76	1.72	1.30	0.94
27R-1, 19–21	713.20	180.00	1.02	0.36	1.73	1.21	0.36
27R-3, 63–65	715.07	138.00	1.03	0.83	1.80	1.24	0.69
28R-1, 36–38	722.87	244.00	1.04	0.02	1.82	1.41	0.30
28R-2, 47–49	724.39	194.00	1.02	0.81	1.82	1.23	0.36
29R-1, 86–88	732.87	135.60	1.03	0.59	1.70	1.30	0.86
30R-1, 106–108	742.57	125.60	1.03	0.53	—	—	—
31R-1, 102–104	752.03	137.90	1.04	0.28	1.56	1.22	0.43
32R-2, 51–53	762.43	117.90	1.03	0.42	1.93	1.22	0.77
32R-4, 75–77	764.07	131.90	1.03	0.78	1.62	1.18	0.32
32R-6, 120–122	765.92	136.80	1.04	0.81	1.87	1.31	0.59
33R-1, 53–55	770.54	181.50	1.06	0.86	1.56	1.44	0.66
37R-1, 133–135	806.84	131.30	1.05	0.56	1.82	1.46	0.65
38R-1, 16–18	815.17	227.40	1.03	0.82	1.89	1.34	0.83
38R-5, 54–56	819.78	180.50	1.04	0.67	1.79	1.26	0.75
40R-1, 130–132	835.31	203.70	1.03	–0.30	—	—	—
40R-4, 5–7	836.88	163.70	1.05	0.95	—	—	—
41R-2, 47–49	845.39	154.00	1.02	–0.03	—	—	—
42R-2, 117–119	855.59	142.80	1.04	0.46	1.76	1.18	0.64
44R-2, 63–65	874.05	240.00	1.01	–0.13	1.89	1.37	0.46
44R-5, 12–14	877.77	177.00	1.48	0.70	1.70	1.50	0.86
45R-4, 53–55	884.87	260.00	1.01	0.63	1.72	1.32	0.87
46R-1, 23–25	891.24	121.50	1.04	0.45	1.68	1.16	0.49

Table T1 (continued). (Continued on next page.)

Core, section, interval (cm)	Depth (mbsf)	AMS			APV		
		K_m (10^{-6} SI)	P_j	T_j	V_m (km/s)	P_j	T_j
46R-5, 78–80	896.01	157.00	1.03	0.83	1.95	1.24	0.58
47R-1, 121–123	901.72	113.00	1.03	0.39	—	—	—
47R-5, 59–61	906.74	127.90	1.05	0.35	—	—	—
48R-1, 13–15	910.14	112.00	1.05	0.36	1.90	1.25	0.43
48R-3, 124–126	914.08	122.00	1.03	0.56	1.80	1.28	0.50
49R-1, 43–45	919.94	102.00	1.04	0.62	1.91	1.27	0.31
49R-4, 63–65	922.96	107.00	1.04	0.41	—	—	—
51R-7, 63–65	946.17	180.00	1.02	0.78	—	—	—
56R-3, 55–57	987.62	95.88	1.02	0.11	—	—	—
57R-1, 6–8	995.57	49.00	1.05	0.13	—	—	—
59R-3, 83–85	1012.20	124.00	1.03	0.25	—	—	—
60R-2, 96–98	1016.40	124.00	1.03	–0.00	—	—	—
61R-1, 96–98	1019.50	108.00	1.03	0.23	—	—	—
61R-5, 33–35	1023.10	168.00	1.04	0.35	—	—	—
62R-1, 35–37	1023.40	106.00	1.02	0.17	—	—	—
62R-CC, 14–16	1026.10	137.40	1.03	0.33	—	—	—
63R-2, 17–19	1034.10	111.00	1.02	0.29	—	—	—
63R-2, 67–69	1034.60	96.00	1.02	0.11	—	—	—
64R-1, 68–70	1042.70	120.00	1.03	0.73	—	—	—
65R-1, 68–70	1047.20	159.00	1.08	0.63	1.85	1.33	0.59
65R-CC, 9–11	1049.50	146.00	1.04	0.60	1.92	1.28	0.51
66R-1, 32–34	1051.30	132.00	1.03	0.68	2.06	1.31	0.83
316-C0004D-							
5R-1, 1–1	137.51	127.7	1.01	0.34	0.14	1.08	0.46
7R-1, 75–75	152.25	98.33	1.01	0.38	0.13	1.11	–0.02
8R-1, 67–67	156.67	178	1.02	0.62	—	—	—
9R-2, 36–36	162.27	289.5	1.02	0.22	0.15	1.12	–0.62
12R-1, 97–97	174.97	136.8	1.02	0.42	0.16	1.13	0.42
13R-CC, 23–23	179.77	176.4	1.02	0.26	0.17	1.16	–0.09
16R-1, 105–105	203.05	207.7	1.01	0.29	0.15	1.07	0.27
17R-CC, 0–0	211.00	146.8	1.02	0.35	0.15	1.05	–0.49
19R-1, 73–73	226.23	336.9	1.01	0.36	0.15	1.08	–0.13
20R-1, 10–10	228.60	179.2	1.01	0.00	0.18	1.07	–0.64
21R-1, 6–6	238.06	350.1	1.01	0.56	0.23	1.14	0.47
25R-CC, 27–27	257.99	184.7	1.01	–0.36	—	—	—
27R-1, 13–13	265.04	174.2	1.01	–0.08	0.16	1.09	–0.11
27R-2, 39–39	266.82	159.8	1.02	–0.44	—	—	—
27R-CC, 11–11	267.49	138.7	1.01	0.18	0.16	1.09	–0.89
27R-CC, 15–15	267.54	237	1.01	0.25	—	—	—
30R-2, 134–134	281.25	285.9	1.01	0.15	0.15	1.05	0.28
32R-1, 4–4	287.53	197.6	1.01	–0.44	0.13	1.12	0.46
37R-1, 2–2	310.02	147.6	1.01	–0.64	0.14	1.07	0.05
37R-2, 27–27	312.36	1920	1.08	0.53	—	—	—
38R-CC, 21–21	315.48	768.2	1.08	0.75	0.13	1.09	0.10
39R-3, 36–36	320.77	359.1	1.09	0.83	0.16	1.40	0.52
40R-1, 59–59	324.08	254.4	1.03	0.51	0.15	1.15	0.46
40R-1, 137–137	324.86	251.5	1.03	–0.19	0.13	1.08	0.25
40R-1, 137–137	324.86	228.5	1.02	0.50	0.13	1.12	0.18
41R-1, 16–16	328.16	309.1	1.03	–0.20	0.13	1.14	0.34
42R-1, 77–77	333.27	489.8	1.03	–0.16	0.15	1.16	0.37
42R-2, 83–83	334.73	254.6	1.03	0.61	0.13	1.11	0.14
42R-3, 76–76	335.67	295	1.03	0.58	0.14	1.15	0.52
43R-1, 83–83	337.83	278.1	1.03	0.20	0.13	1.13	0.26
43R-2, 44–44	338.85	276.8	1.02	0.28	0.14	1.11	–0.26
44R-2, 69–69	343.58	405.8	1.03	0.65	0.13	1.11	0.39
44R-4, 80–80	345.11	397.5	1.05	0.28	0.14	1.16	0.31
45R-1, 42–42	346.42	281	1.02	0.48	0.13	1.06	–0.61
46R-2, 43–43	352.34	598	1.05	0.64	0.16	1.27	0.55
47R-2, 100–100	357.41	417.5	1.02	0.44	0.13	1.06	0.32
48R-2, 84–84	361.74	1041	1.09	0.65	0.17	1.35	0.71
49R-2, 63–63	365.95	409.4	1.05	–0.28	0.19	1.28	0.48
50R-1, 42–42	368.92	1087	1.08	0.47	0.15	1.17	0.52
51R-2, 18–18	374.59	474.6	1.07	0.94	0.15	1.18	0.80
51R-3, 10–10	375.92	420.2	1.06	0.38	0.16	1.15	0.42
52R-1, 38–38	377.98	703.3	1.07	0.46	0.15	1.18	0.34
52R-2, 46–46	379.38	312.5	1.04	0.52	0.14	1.13	0.79
52R-3, 76–76	381.09	617.3	1.05	0.71	0.16	1.13	0.57
53R-1, 45–45	382.45	1398	1.05	0.12	0.16	1.13	0.18

Table T1 (continued). (Continued on next page.)

Core, section, interval (cm)	Depth (mbsf)	AMS K_m (10^{-6} SI)	AMS P_j	AMS T_j	APV V_m (km/s)	APV P_j	APV T_j
53R-2, 13–13	383.54	403.8	1.09	0.69	0.17	1.19	–0.68
54R-1, 95–95	387.45	351.5	1.04	0.20	0.15	1.12	–0.18
54R-3, 53–53	389.84	251.5	1.04	0.76	0.16	1.17	0.66
55R-1, 49–49	391.49	898.3	1.05	0.24	0.13	1.11	0.71
55R-CC, 15–15	394.72	846.6	1.10	0.71	0.16	1.26	0.65
56R-1, 19–19	395.70	439.3	1.08	0.63	0.13	1.14	0.32
56R-CC, 9–9	398.73	292	1.06	0.38	0.18	1.16	0.51
316-C0006E-							
27X-CC, 16–16	201.63	909	1.17	0.67	—	—	—
31X-4, 48–48	233.16	2047	1.08	0.55	1.73	1.15	0.36
31X-0, 32–32	235.71	1430	1.15	0.49	1.59	1.35	0.70
34X-2, 133–133	261.07	1544.5	1.10	0.13	1.80	1.16	0.06
37X-2, 12–12	288.36	1060	1.08	0.11	1.92	1.14	0.37
37X-2, 27–27	288.51	1042	1.12	0.24	1.74	1.29	0.71
37X-6, 29–29	292.78	1800	1.13	0.17	1.74	1.30	0.70
39X-2, 60–60	307.84	809	1.13	0.48	—	—	—
39X-3, 28–28	308.93	1146	1.09	–0.17	1.64	1.16	0.53
39X-5, 41–41	310.48	1658	1.08	0.09	1.68	1.16	0.50
39X-7, 24–24	313.12	2000	1.07	–0.02	1.63	1.17	0.38
39X-8, 15–15	314.45	4293.5	1.06	0.11	1.66	1.22	0.32
40X-1, 29–29	315.61	2224	1.14	0.52	—	—	—
40X-3, 86–86	319.01	1714.5	1.11	0.39	1.79	1.22	0.81
40X-4, 20–20	319.77	2844	1.11	0.35	1.79	1.23	0.58
40X-6, 72–72	321.70	1757.5	1.09	0.23	1.77	1.16	0.64
40X-8, 9–9	322.50	1370	1.10	0.44	—	—	—
41X-3, 17–17	327.83	2788.5	1.11	0.50	—	—	—
42X-1, 36–36	334.69	1657	1.11	0.39	—	—	—
42X-2, 32–32	336.05	1407.5	1.08	–0.62	—	—	—
42X-3, 25–25	337.39	1179	1.19	0.57	1.74	1.39	0.92
42X-7, 32–32	341.70	2026	1.08	0.44	—	—	—
43X-1, 38–38	344.23	2235	1.07	–0.17	—	—	—
43X-2, 112–112	346.36	1340.5	1.10	0.48	1.81	1.15	0.78
43X-6, 96–96	350.45	1319	1.11	0.40	—	—	—
43X-CC, 10–10	352.18	604	1.11	0.71	1.73	1.36	0.76
44X-2, 119–119	355.95	920	1.09	0.40	1.79	1.30	0.67
44X-6, 89–89	360.27	3779.5	1.13	0.35	1.77	1.25	0.29
44X-8, 49–49	362.32	1990	1.10	0.32	—	—	—
45X-3, 24–24	365.87	1898	1.16	0.65	—	—	—
46X-1, 4–4	372.35	91.95	1.01	0.73	—	—	—
46X-2, 68–68	374.43	1615	1.09	0.48	1.87	1.20	0.64
46X-4, 3–3	376.60	1914	1.08	0.41	1.82	1.12	0.18
46X-7, 73–73	380.14	2543	1.07	0.35	—	—	—
46X-CC, 12–12	380.35	2373	1.12	0.38	1.80	1.27	0.43
47X-1, 76–76	382.59	2723.5	1.08	0.05	1.76	1.13	0.51
47X-2, 36–36	383.59	2092	1.09	0.31	—	—	—
47X-3, 121–121	385.86	4282	1.08	0.08	1.62	1.22	0.74
47X-6, 38–38	387.48	3014	1.06	–0.14	1.88	1.16	0.40
47X-7, 56–56	388.05	2556.5	1.06	–0.34	1.86	1.10	0.48
47X-CC, 5–5	391.39	878	1.08	0.24	1.82	1.20	–0.11
48X-3, 53–53	391.78	2299.5	1.07	0.02	1.81	1.13	0.78
48X-2, 14–14	392.88	2066	1.06	0.18	1.76	1.18	0.59
48X-2, 84–84	393.58	1881	1.08	0.11	1.67	1.16	0.51
48X-3, 53–53	394.69	1887	1.05	0.02	1.83	1.19	0.56
48X-4, 121–121	396.79	942	1.08	0.01	—	—	—
49X-1, 80–80	401.63	1770	1.08	0.20	1.83	1.13	0.62
49X-2, 63–63	402.87	1608.5	1.08	0.25	1.81	1.15	0.24
49X-3, 58–58	404.23	2101	1.09	0.40	1.72	1.20	0.45
49X-5, 78–78	405.87	1942	1.17	0.64	—	—	—
316-C0006F-							
1R-1, 47–47	395.47	2637	1.15	0.49	1.88	1.25	0.71
1R-2, 42–42	396.83	2793.5	1.06	0.05	1.81	1.14	0.60
2R-3, 86–86	406.77	1999	1.09	0.27	1.84	1.14	0.32
4R-1, 40–40	423.89	1336.5	1.05	0.11	1.81	1.12	0.54
5R-1, 42–42	433.42	1925	1.05	–0.53	1.81	1.07	0.56
6R-1, 29–29	438.29	433.5	1.05	–0.31	1.81	1.12	0.22
7R-2, 52–52	449.42	329.7	1.04	–0.71	1.78	1.12	0.25
8R-1, 14–14	457.14	296.8	1.05	–0.55	—	—	—

Table T1 (continued). (Continued on next page.)

Core, section, interval (cm)	Depth (mbsf)	AMS K_m (10^{-6} SI)	AMS P_j	AMS T_j	APV V_m (km/s)	APV P_j	APV T_j
9R-1, 34–34	466.84	180	1.03	–0.03	—	—	—
9R-2, 17–17	468.17	138.3	1.01	–0.55	—	—	—
10R-1, 24–24	476.24	300.1	1.02	–0.03	—	—	—
10R-2, 12–12	477.63	527.5	1.05	–0.11	1.81	1.13	0.56
11R-1, 37–37	485.87	194.2	1.02	–0.04	1.57	1.11	0.45
11R-2, 72–72	487.74	188.4	1.01	–0.25	1.72	1.08	–0.16
12R-1, 44–44	495.43	187	1.02	–0.30	1.83	1.13	0.19
12R-1, 47–47	495.46	212.4	1.02	0.18	1.83	1.13	0.50
12R-2, 79–79	497.22	173.2	1.02	–0.24	—	—	—
13R-1, 29–29	504.79	160.7	1.01	–0.14	1.68	1.06	0.11
13R-2, 107–107	506.96	177.7	1.01	–0.34	1.61	1.07	0.74
14R-3, 20–20	517.22	151.5	1.01	–0.51	—	—	—
16R-1, 29–29	533.29	129.8	1.02	–0.51	—	—	—
16R-2, 11–11	534.52	87.9	1.02	–0.19	—	—	—
17R-1, 2–2	542.52	139.1	1.01	–0.12	1.96	1.08	–0.03
17R-CC, 17–17	544.54	125.8	1.02	–0.35	1.94	1.16	–0.20
18R-1, 51–51	552.51	165.7	1.02	0.08	2.01	1.10	0.35
18R-2, 43–43	553.82	171.9	1.02	0.18	1.98	1.14	0.15
19R-1, 13–13	561.63	221.8	1.07	–0.16	1.93	1.14	–0.31
19R-2, 48–48	563.38	180.5	1.02	–0.01	—	—	—
19R-5, 43–43	567.55	160	1.02	–0.19	—	—	—
20R-2, 68–68	573.09	173.7	1.03	0.16	—	—	—
22R-1, 17–17	590.17	159.9	1.02	0.14	1.86	1.13	0.41
23R-1, 75–75	594.25	153.2	1.02	0.24	—	—	—
316-C0007D-							
4R-1, 3–3	199.53	1920	1.04	0.64	—	—	—
9R-1, 21–21	247.21	3750	1.05	0.01	1.53	1.13	0.50
10R-1, 5–5	256.55	2440	1.09	0.00	1.73	1.18	0.51
15R-1, 10–10	303.60	2690	1.13	0.26	1.78	1.18	0.49
15R-1, 77–77	304.27	2410	1.10	0.25	—	—	—
16R-1, 45–45	313.45	1930	1.08	0.40	1.77	1.14	0.55
17R-1, 95–95	323.45	2000	1.10	0.52	—	—	—
17R-2, 40–40	324.27	1230	1.06	0.50	1.80	1.13	0.28
18R-2, 91–91	334.32	1410	1.08	0.23	1.83	1.17	0.38
18R-3, 13–13	334.95	1140	1.07	0.08	1.82	1.18	0.54
19R-1, 11–11	341.61	2050	1.07	0.41	1.84	1.19	0.61
20R-1, 25–25	351.24	2940	1.06	–0.06	—	—	—
20R-2, 90–90	353.32	1720	1.07	0.45	—	—	—
21R-1, 17–17	360.67	6410	1.03	–0.41	1.75	1.11	0.20
22R-1, 84–84	370.84	311	1.02	0.41	1.83	1.08	0.03
22R-3, 73–73	373.55	383	1.02	0.04	—	—	—
22R-4, 8–8	374.34	403	1.03	–0.66	1.80	1.09	–0.34
23R-1, 28–28	379.78	233	1.03	–0.09	1.88	1.11	0.54
23R-1, 121–121	380.71	304	1.03	–0.17	—	—	—
23R-2, 119–119	382.10	244	1.02	0.05	1.79	1.08	–0.17
24R-1, 24–24	389.24	318	1.03	–0.31	—	—	—
24R-1, 77–77	389.77	347	1.05	0.35	1.86	1.17	0.29
24R-3, 56–56	392.40	269	1.04	0.51	1.82	1.14	0.27
24R-4, 48–48	393.72	362	1.01	–0.86	1.85	1.07	–0.75
25R-2, 64–64	400.57	222	1.01	–0.50	1.78	1.13	0.32
25R-4, 77–77	403.54	216	1.02	–0.63	1.78	1.17	–0.11
26R-1, 97–97	408.97	185	1.01	–0.31	1.88	1.09	–0.55
27R-1, 55–55	418.05	—	—	—	1.91	1.16	0.21
28R-2, 91–91	429.33	168	1.02	0.21	—	—	—
29R-1, 87–87	437.37	139	1.02	0.57	1.83	1.14	0.48
29R-2, 85–85	438.76	256	1.02	0.49	1.73	1.08	–0.34
31R-1, 22–22	455.70	326	1.00	0.00	—	—	—
35R-CC, 17–17	484.42	795	1.01	0.06	1.49	1.16	0.41
316-C0008A-							
29X-1, 43–43	225.18	2610	1.08	0.51	—	—	—
29X-4, 62.5–62.5	228.87	838.9	1.05	0.73	1.23	1.14	0.09
30X-2, 54–54	235.81	526.6	1.01	0.62	1.34	1.18	0.44
30X-2, 54–54	235.81	577.1	1.01	0.71	1.33	1.15	0.38
30X-5, 54–54	238.84	547.5	1.03	0.80	1.32	1.18	0.39
31X-1, 105–105	244.80	2984	1.08	0.42	1.28	1.18	0.04
31X-5, 50–50	249.46	297.1	1.03	0.63	1.33	1.28	0.42
31X-9, 100–100	253.93	2039	1.11	0.73	1.43	1.27	0.46

Table T1 (continued).

Core, section, interval (cm)	Depth (mbsf)	AMS			APV		
		K_m (10^{-6} SI)	P_j	T_j	V_m (km/s)	P_j	T_j
32X-6, 83–83	258.18	858.9	1.11	0.35	1.48	1.31	0.55
32X-4, 105–105	260.60	1645	1.04	0.13	—	—	—
33X-1, 76–76	263.51	1592	1.09	0.69	1.46	1.09	0.36

AMS = anisotropy of magnetic susceptibility, APV = anisotropy of *P*-wave velocity, K_m = mean magnetic susceptibility, P_j = Jelinek anisotropy parameter, T_j = Jelinek shape parameter, V_m = mean *P*-wave velocity (see "Methods").